electronics

MDPI

Review

Review of the Comprehensive SAR Approach to Identify Scattering Mechanisms of Radar Backscatter from Vegetated Terrain

Motofumi Arii [1,*], Hiroyoshi Yamada [2], Shoichiro Kojima [3] and Masato Ohki [4]

[1] Mitsubishi Space Software Co., Ltd. Kamakura 247-0065, Japan
[2] Department of Information Engineering, Niigata University, Niigata 950-2181, Japan; yamada@ie.niigata-u.ac.jp
[3] Applied Electromagnetic Research Institute, National Institute of Information and Communications Technology, Tokyo 184-8795, Japan; skojima@nict.go.jp
[4] Earth Observation Research Center, Japan Aerospace Exploration Agency, Tsukuba 305-8505, Japan; ohki.masato@jaxa.jp
* Correspondence: Arii.Motofumi@mss.co.jp

Received: 28 June 2019; Accepted: 27 September 2019; Published: 29 September 2019

Abstract: In a field of polarimetric synthetic aperture radar (SAR) remote sensing, various kinds of polarimetric decomposition techniques have been proposed. However, poor validations prevent them from operational applications. A true composition ratio of scattering mechanisms within a radar backscatter plays a key role. To overcome the issue, a novel comprehensive SAR approach to accurately identify a contribution of each scattering mechanism has been introduced. This is based on multiparametric SAR observation combined with a numerical model simulation. In this article, a comprehensive SAR approach is concisely reviewed to accelerate the research in this field. First, popular model-based polarimetric decompositions are introduced and their limitations are shown. Then, a behavior of scattering mechanisms is analyzed by the discrete scatterer model with some results using real multiparametric SAR data. A comprehensive SAR approach must be essential to realize an operational use of polarimetric SAR data.

Keywords: comprehensive SAR; multiparametric SAR observation; discrete scatterer model

1. Introduction

One of the main motivations of polarimetric synthetic aperture radar (SAR) remote sensing is to invert physical information from radar signal from vegetated terrain. Its flexible operability and an obvious sensitivity to a vegetation structure make polarimetric SAR an attractive monitoring tool [1–11]. A full polarimetric SAR capability such as Advanced Land Observing Satellite-2 (ALOS-2), developed by the Japan Aerospace Exploration Agency, has been universal in these days, and so various polarimetric decomposition techniques have been proposed [11–20]. Nonetheless, the decomposition techniques still have never been recognized as a solid practical application even after 30 years.

The backscattering cross section from vegetated terrain consists of various scattering mechanisms [21]. Simple forest model in Figure 1 generates a number of scattering mechanisms such as volume scattering from canopy or trunks, double-bounce scattering between canopy and ground or between trunk and ground, and surface scattering. In addition, the scattering mechanisms passing through a volume layer of leaves, twigs or trunks are attenuated [22,23], and of course, there are a large number of multiple scatterings within a layer. The variation makes an inversion of physical parameters seriously complicated. Suppose that a more backscattering cross section would be observed in a forest after rain. It could be explained by a mixture of various hypotheses such as a growth of vegetation,

increased vegetation water content, increased soil moisture under vegetation, varied vegetation structure, and so forth. Each hypothesis must be tightly connected to a different set of scattering mechanisms in Figure 1 so that it could be difficult to directly retrieve physical parameters such as soil moisture, vegetation water content, and biomass without knowing a portion of scattering mechanisms.

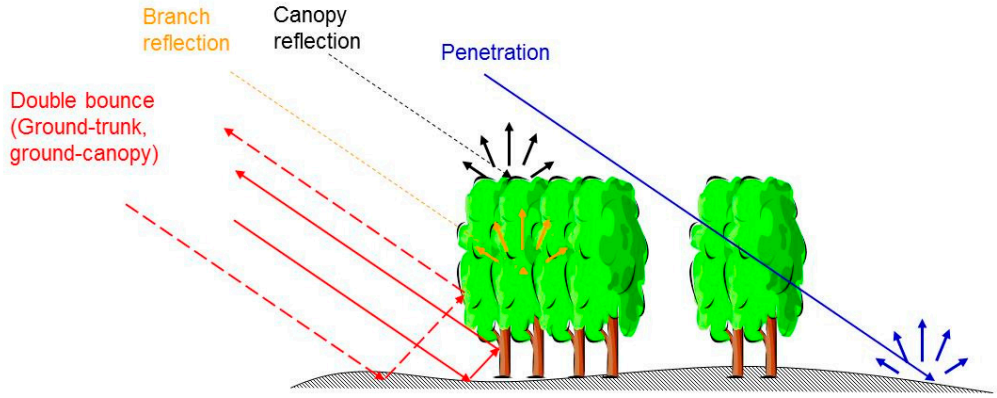

Reprinted, with permission, from Arii, M. Soil moisture retrieval under vegetation using polarimetric radar. Ph.D. Thesis, California Institute of Technology, 2009.

Figure 1. Backscattering from a vegetated terrain [21].

Main motivation to introduce full polarimetric SAR is to understand radar backscatter based on scattering mechanisms, and this leads to a potential problem. Unfortunately, there is no way to directly measure a composition ratio of scattering mechanisms within radar backscatter so that only a limited validation has been conducted to polarimetric decomposition results. This could prevent the polarimetric decomposition, even polarimetric SAR data, from being widely established.

To overcome the issue, a forward model, which theoretically calculates backscatter from randomly vegetated terrain, has been introduced [15,21,24–26]. The model simply provides us a contribution of each scattering mechanism in terms of specific observation condition such as the incidence angle and polarization so that one can quantitatively compare a set of experimental data with the numerical simulation results. The radar backscatter could be precisely characterized.

Forward models generally have a high degree of freedom so that many parameters must be reasonably determined. For this purpose, a multiparametric SAR observation, where various observation conditions such as frequency, polarization and incidence angle are gradually varied in a wide range of each value during a short span of time, has been proposed [27–36]. Simulation parameters can be found by fitting the model to the series of data set obtained by the multiparametric SAR observation. This comprehensive SAR approach can provide reliable model parameters.

In this article, essential elements for the comprehensive SAR approach are concisely reviewed to accelerate the research in this field. First, popular model-based polarimetric decompositions are introduced and their limitations are shown. Then, forward models are reviewed with real SAR data based on a multiparametric SAR observation. Note that the main part of this review article is based on our previous works [18,19,21,32,34,36,37].

2. Model-Based Polarimetric Decompositions and Their Limitation

Most polarimetric decomposition techniques proposed for nearly three decades could be categorized into two groups. An eigenvector-based decomposition was introduced by Cloude in the context of radar imaging [12] and the other researchers follow [13,16]. This method always provides a unique solution mathematically, whereas some approximations must be required to interpret the results in terms of established physical scattering mechanisms as described in [13].

Model-based polarimetric decomposition, as proposed by Freeman and Durden [14], is another group. There are three well-known physical scattering mechanisms: A volume scattering from canopy, a double-bounce scattering between tree and surface and a backscattering from the ground. The authors proposed that the measured covariance matrix can be expressed by a linear sum of them. Due to its simplicity, this method has been widely used. Our original purpose to introduce the polarimetric decomposition technique was to understand the behavior of physical scattering mechanisms so that the model-based polarimetric decomposition would be reviewed in the rest of this article.

The Freeman and Durden algorithm can decompose an observed covariance matrix of C to three elemental scattering mechanisms as:

$$\langle [C] \rangle = f_v \langle [C_v] \rangle + f_d [C_{db}] + f_s [C_s], \tag{1}$$

where f_v, f_d and f_s are coefficients of volume, double-bounce and surface scattering, respectively, whereas C, C_v, C_{db} and C_s are covariance matrices of total, volume, double-bounce and surface scatterings, respectively. Note that < and > indicates the ensemble average of adjacent pixels. Now the algorithm in [14] was applied to real SAR data of Black Forest in Germany, obtained by the National Aeronautics and Space Administration/Jet Propulsion Laboratory (NASA/JPL) Airborne Synthetic Aperture Radar (AIRSAR) system in the summer of 1991, shown in Figure 2.

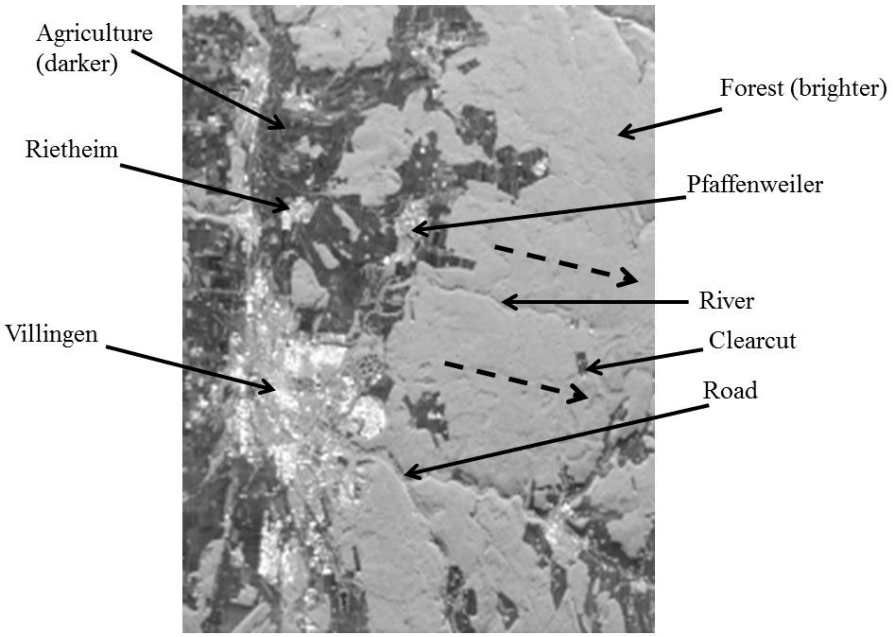

© Courtesy NASA/JPL-Caltech.
Reprinted, with permission, from Arii, M. Soil moisture retrieval under vegetation using polarimetric radar. Ph.D. Thesis, California Institute of Technology, 2009.

Figure 2. L-band image of the Black Forest in Germany obtained by the NASA/JPL AIRSAR system in the summer of 1991. The solid arrows indicate the name of city or area type. The dotted lines specify the direction of topographic change. The terrain slopes upward in the direction of the arrows [21].

The observations at C-band (6 cm), L-band (24 cm) and P-band (68 cm) were conducted, and a portion of three scattering mechanisms is shown in Figure 3.

The double-bounce component clearly discriminates urban areas such as Villingen and Rietheim for all wavelengths. A good penetration of canopy layer was obviously shown by the longer wavelengths in the agricultural area, and double-bounce scattering appears instead of the volume component.

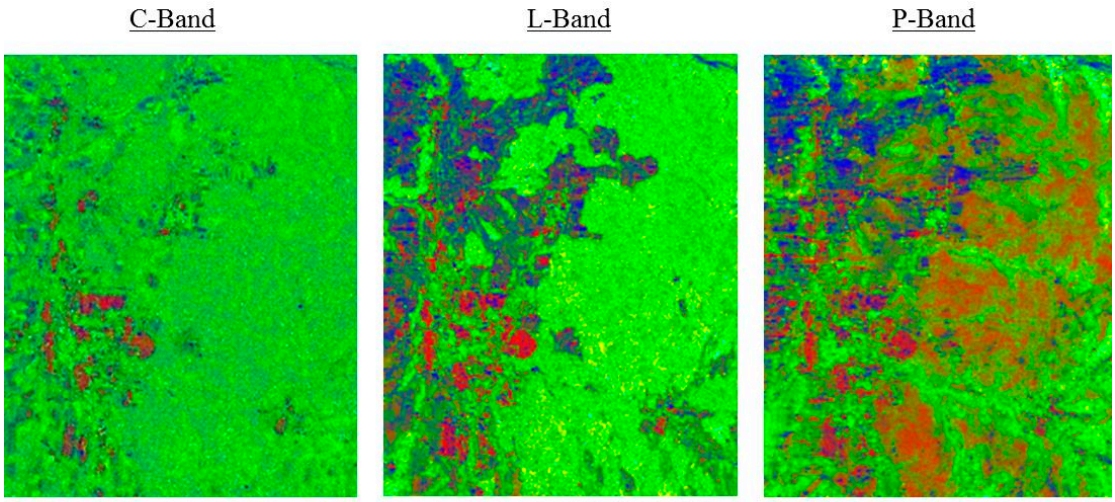

Reprinted, with permission, from Arii, M. Soil moisture retrieval under vegetation using polarimetric radar. Ph.D. Thesis, California Institute of Technology, 2009.

Figure 3. Results of the Freeman algorithm applied to three different wavelength images in Freiburg obtained by AIRSAR. From left to right, C-band (5 cm), L-band (24 cm) and P-band (68 cm) images are displayed. Green, red and blue are assigned to volume scattering, double-bounce scattering and ground scattering, respectively [21].

The Freeman and Durden algorithm sometimes breaks a conservation law of energy so that negative power could be estimated for a term on the right-hand side of Equation (1) as discussed in [18]. Since the algorithm by Freeman assumes that all of cross-polarization term is automatically assigned to the volume component, it may underestimate the contribution from other scattering mechanisms. Therefore, van Zyl et al. introduced Equation (2) to investigate a pixel having negative power [18]:

$$[C_{remainder}] = \langle [C] \rangle - f_v \langle [C_v] \rangle. \quad (2)$$

The negative power in Equation (2) can be easily obtained through eigenvalue analysis [18], and a result is shown in Figure 4 where pixels having negative power are indicated by black color. Unfortunately, most of the negative power happened in the forested area.

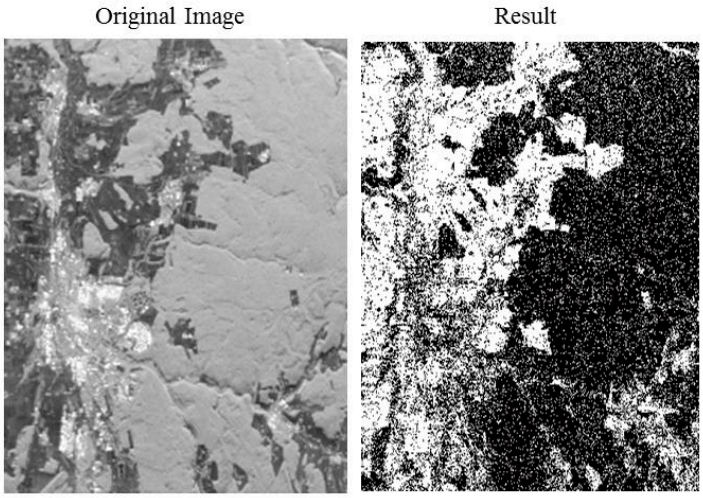

Reprinted, with permission, from Arii, M. Soil moisture retrieval under vegetation using polarimetric radar. Ph.D. Thesis, California Institute of Technology, 2009.

Figure 4. Pixels with negative eigenvalue are displayed using the L-band Black Forest image. The left image is the total power image at L-band, and the right image is the result of the validation test [21].

The negative power distributed at most of the forested area was physically unacceptable. For this violation of physics, the nonnegative eigenvalue decomposition (NNED) model [18] has been proposed as follows:

$$\langle [C] \rangle = f_v \langle [C_v] \rangle + f_d [C_{db}] + f_s [C_s] + [C_{reminder}]. \quad (3)$$

By combining the remainder term with the eigenvalue decomposition technique [18], the three-component model guarantees that any term on the right-hand side of Equation (3) would be positive semidefinite. The result by the NNED is shown in Figure 5.

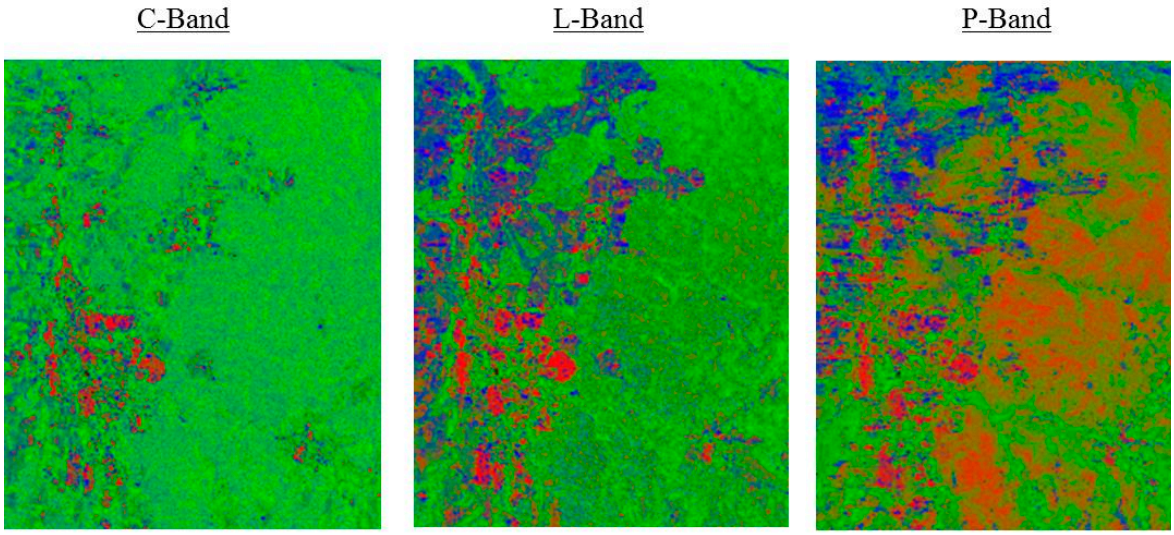

Reprinted, with permission, from Arii, M. Soil moisture retrieval under vegetation using polarimetric radar. Ph.D. Thesis, California Institute of Technology, 2009.

Figure 5. Decomposition results using nonnegative eigenvalue decomposition (NNED) are shown. The original images with three different frequencies are the same as in Figure 3. Color assignments are the same as Figure 3 as well [21].

It can be easily seen that the volume scattering component was distinctly reduced whereas surface scattering and double-bounce scattering were exaggerated in the images at L- and P-bands, respectively. Some faint red was recognized in the middle of the Black Forest at L-band. Any difference between the two techniques could not be seen in the agricultural and urban areas. The volume scattering component was also still recognized around the river halfway down the image at the P-band.

As mentioned in [19,37], the decomposition techniques shown above were operated on a pixel-to-pixel basis, either supposing the same volume scattering component for an entire image or utilizing a limited number of scattering models (three in the case of Yamaguchi et al. [15]) to select for each pixel. Randomly distributed dipoles are generally assumed to calculate a volume scattering component, where probability distribution function (pdf) of their orientation angle is specified. For example, Freeman and Durden algorithm utilizes a volume scattering component as follows:

$$\langle [C_v] \rangle = \begin{bmatrix} 3 & 0 & 1 \\ 0 & 2 & 0 \\ 1 & 0 & 3 \end{bmatrix}. \quad (4)$$

This assumes uniformly distributed thin cylinders so that the model disagrees to a pixel having methodically distributed thin cylinders with distinct mean orientation angle. To conquer the limitation, Arii et al. completely generalizes the volume component models:

$$\begin{aligned}
\langle [C_v(\theta_0,\sigma)] \rangle &= [C_\alpha] + p(\sigma)\left[C_\beta(2\theta_0)\right] + q(\sigma)\left[C_\gamma(4\theta_0)\right], \\
[C_\alpha] &= \frac{1}{8}\begin{bmatrix} 3 & 0 & 1 \\ 0 & 2 & 0 \\ 1 & 0 & 3 \end{bmatrix}, \\
\left[C_\beta(2\theta_0)\right] &= \frac{1}{8}\begin{bmatrix} -2cos2\theta_0 & \sqrt{2}sin2\theta_0 & 0 \\ \sqrt{2}sin2\theta_0 & 0 & \sqrt{2}sin2\theta_0 \\ 0 & \sqrt{2}sin2\theta_0 & 2cos2\theta_0 \end{bmatrix}, \\
\left[C_\gamma(4\theta_0)\right] &= \frac{1}{8}\begin{bmatrix} cos4\theta_0 & -\sqrt{2}sin4\theta_0 & -cos4\theta_0 \\ -\sqrt{2}sin4\theta_0 & -2cos4\theta_0 & \sqrt{2}sin4\theta_0 \\ -cos4\theta_0 & \sqrt{2}sin4\theta_0 & cos4\theta_0 \end{bmatrix},
\end{aligned} \tag{5}$$

where θ_0 and σ are the mean orientation angle and pdf of the randomly distributed dipoles, respectively. Both p and q are predetermined functions in terms of σ [37]. One of the most significant merits of this model was that any volume component could be expressed by only two parameters, θ_0 and σ, which were related to physical vegetation as shown in Figure 6.

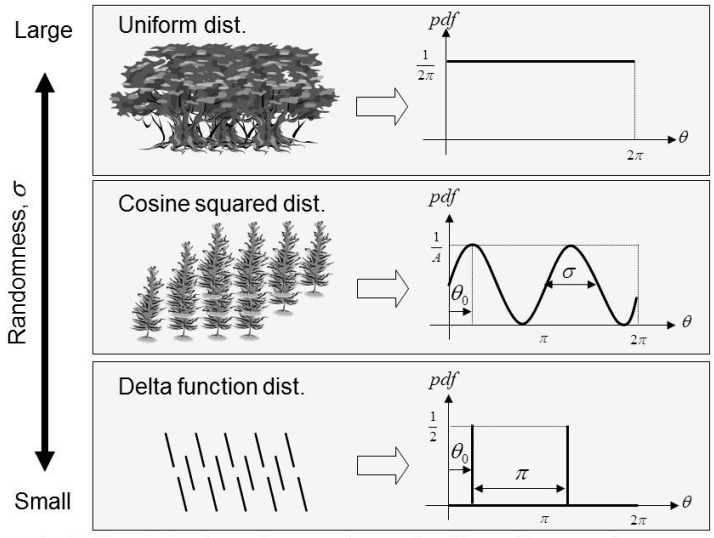

© 2019 IEEE. Reprinted, with permission, from Arii, M.; Yamada, H.; Kobayashi, T.; Kojima, S.; Umehara, T.; Komatsu, T.; Nishimura, T. Theoretical characterization of X-band multi-incidence angle and multi-polarimetric SAR data from rice paddies at late vegetative stage. IEEE Trans. Geosci. Remote Sens., 2017, 55, 2706-2715.

Figure 6. Various probability distribution functions (pdfs) in terms of randomness. There are two extreme cases: Uniform distribution with the highest variance and delta function distribution with the lowest variance. Cosine squared distribution sits in between these two. The randomness is defined by σ as shown in the cosine squared distribution [32].

Adaptive NNED (ANNED) technique has been realized by introducing the generalized volume scattering component as follows:

$$\langle [C] \rangle = f_v \langle [C_v(\theta_0,\sigma)] \rangle + f_d[C_{db}] + f_s[C_s] + [C_{reminder}]. \tag{6}$$

To fix the additional parameters θ_0 and σ, the remainder term is again utilized to avoid negative power [19]. A result by the adaptive model for the Black Forest data is shown in Figure 7.

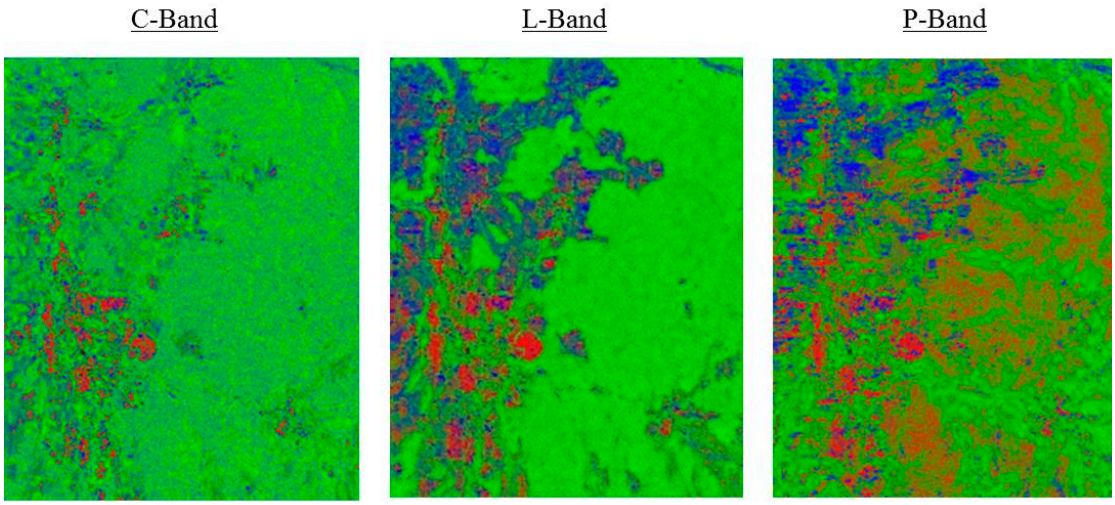

Reprinted, with permission, from Arii, M. Soil moisture retrieval under vegetation using polarimetric radar. Ph.D. Thesis, California Institute of Technology, 2009.

Figure 7. Results of the ANNED algorithm applied to three different wavelength images in Freiburg obtained by AIRSAR. Green, red and blue are assigned to the volume, double bounce and ground components [21].

Much more of the volume scattering contribution can be recognized in the forested area from the ANNED results at L-band whereas a similar tendency can be seen around the river halfway down the image at the P-band. The remainder term of Equation (6) was mapped to further study the applicability of ANNED in Figure 8 at the L-band. By supposing two different distributions: Uniform and cosine squared having no orientation angle for the volume scattering model, the results of NNED and ANNED were compared. The model tells that the smaller value in pixel in Figure 8 would be considered as the better fit to the selected parameters of the model.

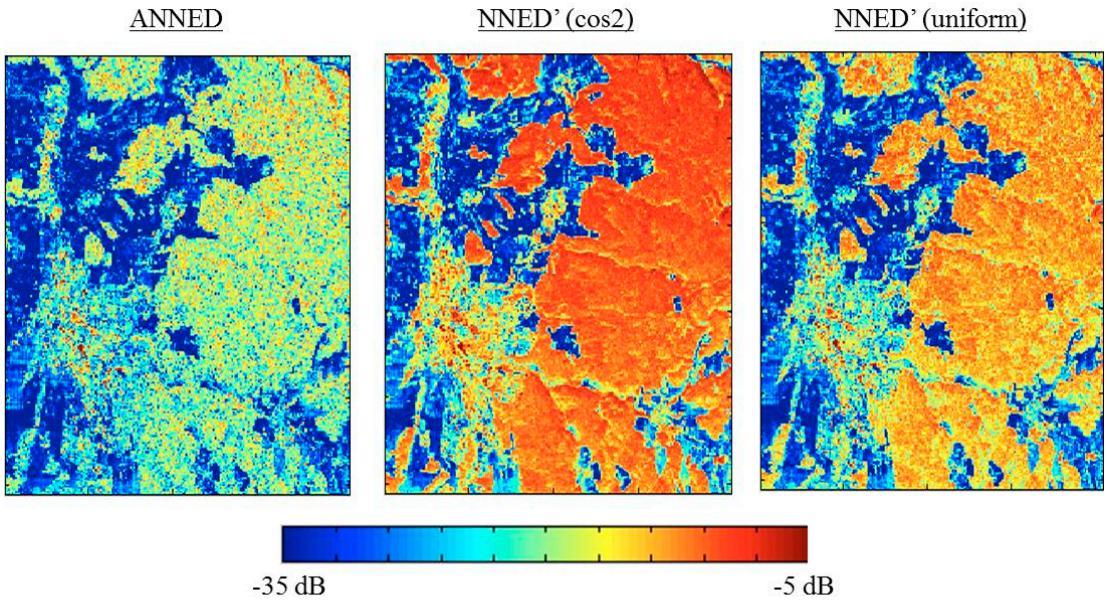

Reprinted, with permission, from Arii, M. Soil moisture retrieval under vegetation using polarimetric radar. Ph.D. Thesis, California Institute of Technology, 2009.

Figure 8. $C_{remainder}$ of ANNED (left) for the L-band Black Forest image compared with those of NNED' (dash) using two distributions: cosine squared (center) and uniform (right) distribution. Note that the cosine squared distribution has a zero orientation angle [21]. Note that NNED' is an extended version of NNED so that reflection symmetry [38] is never required.

This shows that the best fit parameter set could be reasonably found by ANNED especially in the forested area. Therefore, it should be concluded that an excellent applicability to the various vegetated surfaces were realized by ANNED. The results obtained by ANNED from multipolarization and multifrequency SAR data were qualitatively validated.

In [32], Arii et al. have first applied the model-based polarimetric decomposition technique to real multi-incidence angle and multi-polarimetric SAR (MIMP SAR) data sets from rice paddies at the X-band obtained by Pi-SAR2 developed by the National Institute of Information and Communications Technology. Contribution of each scattering mechanism derived by the Freeman and Durden algorithm is shown in Figure 9.

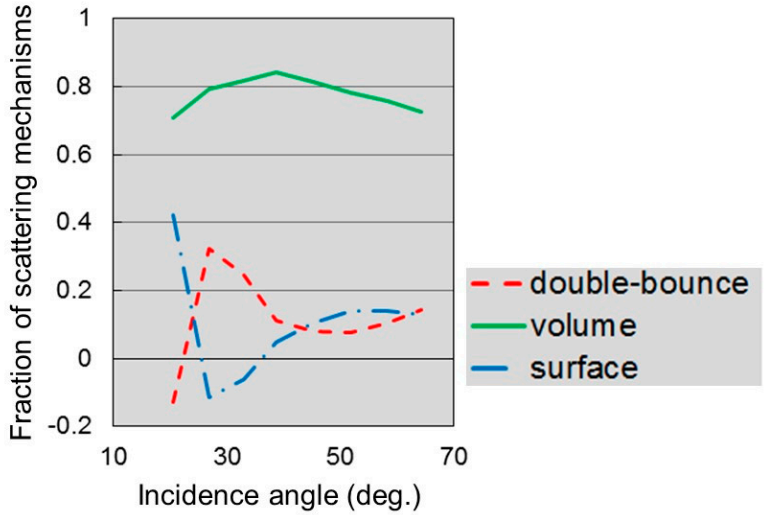

© 2019 IEEE. Reprinted, with permission, from Arii, M.; Yamada, H.; Kobayashi, T.; Kojima, S.; Umehara, T.; Komatsu, T.; Nishimura, T. Theoretical characterization of X-band multi-incidence angle and multi-polarimetric SAR data from rice paddies at late vegetative stage. IEEE Trans. Geosci. Remote Sens., 2017, 55, 2706-2715.

Figure 9. Freeman and Durden's three-component scattering decomposition result for block D [32].

It was obvious that the only dominant scattering mechanism over an entire range of incidence angles was the volume scattering. As previously mentioned, this is caused by all of HV, where vertically polarized wave is transmitted and horizontally polarized wave is received, being blindly considered as the volume scattering element. Therefore, as shown in the figure, negative power might occur if significant HV was obtained. Moreover, interaction between rice crops and ground surfaces and surface scattering alternate in terms of incidence angles. Only with a 10-degree difference of incidence angles that the second most dominant scattering was exchanged. A phase of the correlation between HH, where horizontally polarized wave is transmitted and received, and VV, where vertically polarized wave is transmitted and received, could be a potential reason because the phase plays a key role to estimate the amount of a double-bounce scattering and surface scattering by most of the model-based polarimetric decomposition techniques such as the three-component scattering decomposition [14,15,18,19]. The algorithm may not properly work if a dominant scattering mechanism to each co-polarization becomes different.

It could be an issue that the analysis above cannot be deepened any more without knowing the true fraction of each scattering mechanism. In addition, there were several critical oversights in the polarimetric decomposition models. First, attenuation by the volume layer was never taken into account. As shown in [21,29], attenuation may dictate backscatter from vegetated terrain when the amount of scatterers in a volume layer exceeds a certain amount. Second, a volume scattering component was estimated by assuming a thin cylinder, that is, dipoles, even though, natural scatterers are generally more like cylinders with a certain thickness. With the current decomposition models, a number of unknown parameters were more than those of polarimetric SAR observations. To make

SAR remote sensing an effective tool to monitor vegetated surfaces, an accurate fraction of scattering mechanisms to compare with the observation becomes essential.

3. Comprehensive SAR Approach

There is no way to directly measure the individual scattering mechanism within radar backscatter from vegetated terrain. To obtain an accurate fraction of scattering mechanisms, a forward model numerically calculating a contribution of each scattering mechanism was introduced. The model usually has a high degree of freedom so that many parameters have to be predetermined. The authors also have proposed multiparametric SAR observation that monitors a specific target by gradually varying the observation conditions so that the model parameters could be accurately estimated by comparing with a set of observation data. In this section, both technical elements, that is, a forward model and multiparametric SAR observation, were explained as essential elements of a comprehensive SAR approach.

3.1. Forward Model

To describe radar backscatter from vegetated surfaces, there are two models widely used. One is a radiative transfer model consisting of the layer structure, and the other is a discrete scatterer model (DSM) consisting of randomly distributed scatterers.

Chandrasekhar [39] originally introduced the radiative transfer theory. Then the concept was successfully applied to radar scattering from vegetated surfaces by Ulaby et al. [40–43]. This model is called Michigan microwave canopy scattering (MIMICS), in which a three-layer structure is considered in a typical forest, that is, the canopy layer, trunk layer and ground layer, with border condition. Differential equations can be formed to model the net intensity for each of the upward and downward directions within a layer by assuming the conservation law of energy for the infinitely thin slab. The backscattering cross section can be obtained by integrating the thin slab over an entire layer structure to the height direction under border conditions. Multiple scattering considered in the MIMICS causes higher accuracy than the DSM whereas the MIMICS may not provide sufficient physical insight due to its complexity. The other models based on radiative transfer are also discussed in [44,45].

Durden et al. proposed the DSM in [25] assuming the model for vegetated terrain as shown in Figure 10.

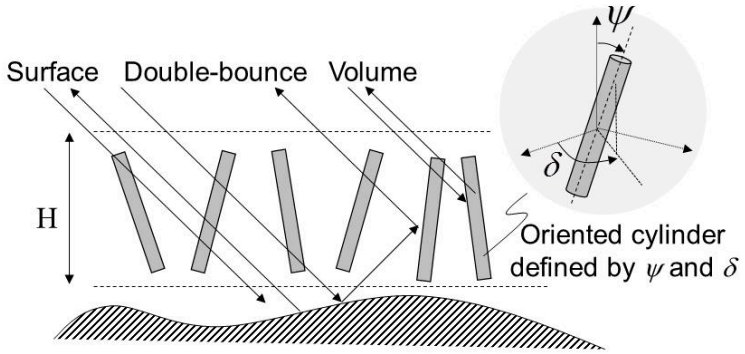

© 2019 IEEE. Reprinted, with permission, from Arii, M.; Yamada, H.; Kobayashi, T.; Kojima, S.; Umehara, T.; Komatsu, T.; Nishimura, T. Theoretical characterization of X-band multi-incidence angle and multi-polarimetric SAR data from rice paddies at late vegetative stage. IEEE Trans. Geosci. Remote Sens., 2017, 55, 2706-2715.

Figure 10. Various scattering mechanisms, volume, double-bounce and surface scatterings, from a cloud of oriented cylinders on the ground. An orientation of each cylinder is defined by ψ (elevation) and δ (azimuth) [32].

The model was filled up with discrete scatterers, and their multiple scatterings were ignored. Since the scatterers inside the canopy were assumed to be sparsely distributed, the scattered wave could be attenuated well through multiple scatterings [21,22]. Based on this assumption, the only three distinct scattering mechanisms such as volume scattering, interaction between the ground and volume scatterers and surface scattering describe the model.

Randomly oriented thin cylinders on the dielectric surfaces were assumed by the DSM as described in Figure 10. Surface scattering [46], double-bounce scattering, and volume scattering [47–49] were incoherently integrated by considering attenuations given by an optical theorem caused by randomly distributed elemental scatterers [22]. Randomly oriented thin cylinders were expressed not only by the cylinder distribution but also by the mean orientation angle and randomness as described in Figure 6. The randomness, σ, had a range of 0 (Delta function distribution: Methodical distribution) and 0.91 (uniform distribution) as a standard deviation, whereas the mean orientation angles, θ_0, appeared at every 180°. Note that a cosine squared distribution corresponds to the randomness of 0.56 as a medium randomness. In addition to the use as a validation tool of the polarimetric decomposition technique, the model could be directly utilized to invert physical parameters such as soil moisture as shown in [21,24,35].

To demonstrate a data analysis based on the DSM, rice paddies at late vegetative stage are modeled for example [32,34,36]. Three scatterers such as a grain, a stem and a leaf have been taken into account as elements of rice paddies at late vegetative stage. Leaves and stems are assumed to be in the same layer, whereas grains are on the top layer. The two-layer model with three types of distributed elemental scatterers is conceptually expressed in Figure 11.

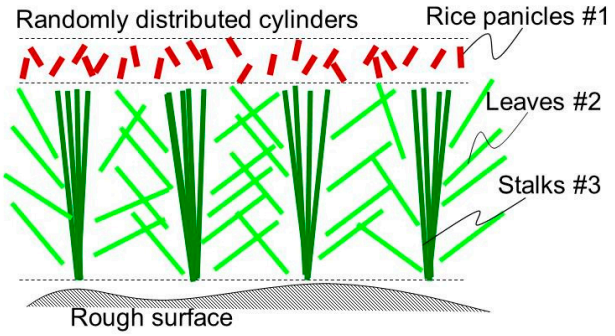

© 2019 IEEE. Reprinted, with permission, from Arii, M.; Yamada, H.; Kojima, S.; Ohki, M. Sensitivity analysis of multifrequency MIMP SAR data from rice paddies. IEEE Trans. Geosci. Remote Sens., 2019, 57, 3543-3551.

Figure 11. Schematic model for the discrete scatterer model (DSM). Randomly distributed cylinders stand on the dielectric rough surfaces [36].

An incoherent model cannot express a coherent effect such as radio interferometry. The effect could be significant on backscatter from densely distributed rice plants, where each scatterer is much smaller than the wavelengths. In this case, in-situ measured data should not be directly used as a set of input parameters, because backscatter from each element could be considerably weak so that incoherently summed power from all of the plants still stays weak. To explain certain scattering power by the incoherent model, a radio interferometry is realized by clustering the densely distributed thin scatterers at a scale of wavelength. The ears of rice plants at this stage form a slender cluster, which can be simply expressed as a virtual cylinder. The same concept is applied to leaves and stalks, bunches of which could be described as virtual cylinders, as shown in Figure 12.

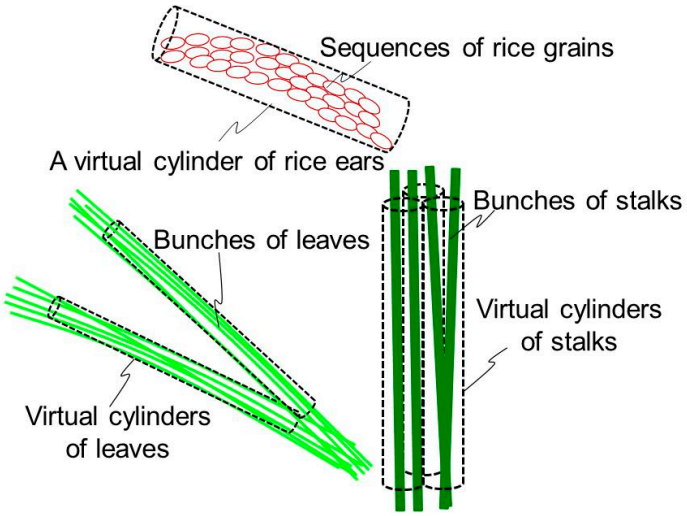

© 2019 IEEE. Reprinted, with permission, from Arii, M.; Yamada, H.; Kojima, S.; Ohki, M. Sensitivity analysis of multifrequency MIMP SAR data from rice paddies. IEEE Trans. Geosci. Remote Sens., 2019, 57, 3543-3551.

Figure 12. Cylinder models of sequences of rice ears, bunches of leaves and bunches of stalks [36].

The model allows calculating backscattering cross section at different bands so that multifrequency data analysis can be conducted. In this example [36], two blocks, A and B, of rice paddies were selected, and each block is simulated at the X- and L-bands. Table 1 shows model input parameter sets for XA, XB, LA and LB, which are determined by experimentally obtained SAR data (X-band on August 21, 2014 and L-band on August 3, 2016) as described in the Section 3.2. Note that the volumetric water content of each element is related to the dielectric constant by the Dual-dispersion model proposed in [50], where dielectric constants corresponding to 5% and 35% at X-band, and 12%, 15%, and 31% at the L-band of volumetric water contents are 3.1 and 17.2 at X-band, and 8.7, 10.7 and 21.0, respectively. The volumetric water contents in Table 1 may imply dryer vegetation condition than those shown in [51–53]. Since the dielectric constant at the center of a trunk is much higher than that on the surface as experimentally shown in [54], backscatter from rice paddy could be characterized as dryer condition than its true vegetation water content if the incident wave would not reach to a center of a grain, a stalk or a leaf.

Table 1. Model input parameters [36].

Parameter	Value XA	Value XB	Value LA	Value LB
Incidence angle (deg.)	25–65	25–65	24–55	24–55
Wavelength (cm)	3	3	24	24
Stem	-	-	-	-
Volumetric water content (%)	5	5	12	12
Radius (mm)	1.0	1.0	16	16
Layer height (m)	0.80	0.80	0.60	0.60
Mean orientation angle (deg.)	0.0	0.0	2.0	2.0
Distribution	0.40	0.40	0.30	0.30
Density (m^{-3})	400	400	150	150
Length (cm)	80	80	42	42
Leaf	-	-	-	-
Volumetric water content (%)	5	5	15	15
Radius (mm)	1.0	1.0	3.0	3.0
Layer height (m)	0.80	0.80	0.60	0.60
Mean orientation angle (deg.)	43	43	80	80
Distribution	0.42	0.42	0.30	0.30
Density (m^{-3})	1200	1200	700	700
Length (cm)	35	35	90	90

Table 1. *Cont.*

Parameter	Value XA	Value XB	Value LA	Value LB
Grain	-	-	-	-
Volumetric water content (%)	35	35	31	31
Radius (mm)	2.6	2.6	16.8	17.3
Layer height (m)	0.20	0.20	0.30	0.30
Mean orientation angle (deg.)	76	76	0.0	0.0
Distribution	0.38	0.38	0.09	0.088
Density (m^{-3})	500	500	430	430
Length (cm)	10.0	10.0	4.5	4.5
Volumetric soil moisture (%)	6	6	31	31
Surface roughness (mm)	0.2	0.2	1.0	1.0
Correlation length (mm)	5	5	20	20

© 2019 IEEE. Reprinted, with permission, from Arii, M.; Yamada, H.; Kojima, S.; Ohki, M. Sensitivity analysis of multifrequency MIMP SAR data from rice paddies. IEEE Trans. Geosci. Remote Sens., 2019, 57, 3543–3551.

Backscattering cross sections in terms of polarization, incidence angle and frequency are numerically calculated by the DSM as shown in Figure 13.

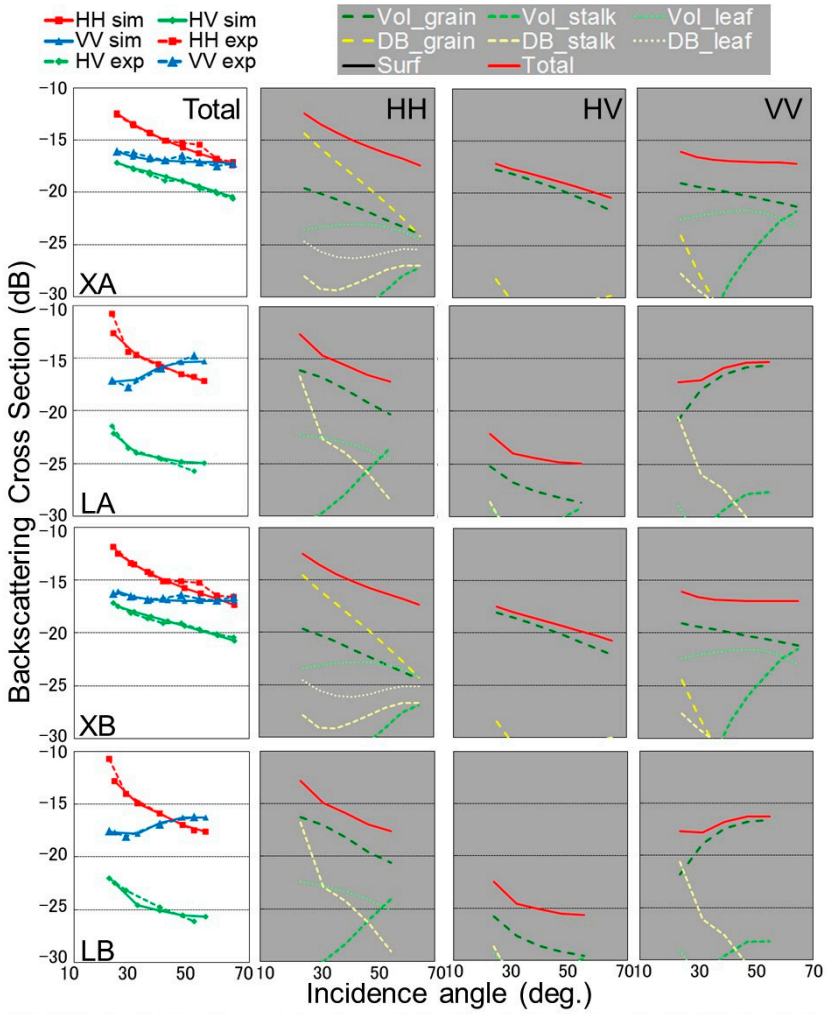

© 2019 IEEE. Reprinted, with permission, from Arii, M.; Yamada, H.; Kojima, S.; Ohki, M. Sensitivity analysis of multifrequency MIMP SAR data from rice paddies. IEEE Trans. Geosci. Remote Sens., 2019, 57, 3543-3551.

Figure 13. Comparison of the experimental data and DSM simulation results on blocks A and B at the X- and L-bands (left). Contribution of each scattering mechanism is also shown on the right-hand side with respect to polarization [36].

Based on the DSM modeling described in [32,34,36], each scattering mechanism is contributed to the total power as also shown on the right-hand side in Figure 13. The most dominant for all polarizations except HH is the volume scattering from rice panicles at the X-band, where interaction between grains and the surfaces is dominant. Another interaction between stalks and the ground surfaces is also dominant for HH and VV only at small incidence angles at the L-band. The most complicated curve is formed by VV at the X-band because the total power is pushed up by the volume scatterings from grains, leaves and stalks in terms of incidence angles one after another. Although numerical simulations by another set of input parameters assigning dominant vegetation water content to stem or leaf were conducted, strong attenuation of upper layer with rice panicles prevents from finding a set of input parameters to reasonably explain the observations. Nonetheless, it must be noted that the simulation results may not be a unique solution so that the interpretation could be varied by using a different forward model or a different set of input parameters.

Radius is the grain parameter with the most significant gap between the X- and L-bands, as shown in Table 1. In [49], scattering from a cylinder can be theoretically characterized by a wave number, k, and a cylinder radius, r, so that the kr must be conserved at different wavelengths as long as a received power stays at same level. This happened in the observation on HH and VV in Figure 13. The radii of virtual cylinders of grains at the L- and X-bands are 17.3 mm and 2.6 mm so that the ratio (17.3:2.6 mm) is approximately comparable to the ratio of the wavelength of the L-band to that of the X-band (24:3 cm). Therefore, the ratio of the radius to the wavelength is almost conserved. Based on the analysis, the effective radius of a virtual cylinder of rice grains at the late vegetative stage would vary due to the wavelength in use.

Clearly, the visible breakdown of the individual scattering mechanism in terms of polarization, frequency, and the incidence angle could deepen our understanding. The DSM could be an essential candidate of tools to provide a visible fraction among scattering mechanisms.

3.2. *Multiparametric SAR Observation*

The simulation results in the previous section show that a distinct sensitivity of the backscattering cross section from vegetated terrain to a various observation parameter is indicated. On the other hand, the DSM has a high degree of freedom so that it consists of many physical parameters as shown in Table 1. It is crucial to find a set of simulation parameters to reasonably describe the behavior of each scattering mechanism for an entire range of the observation condition.

To fix the model parameters, a great advantage potentially exists on MIMP-SAR data [32,34]. Although only a single point must be interpreted by a single incidence angle and single-polarimetric SAR observation, the MIMP SAR observation can provide multiple continuous curves in terms of incidence angles on each polarization. A few decades ago, it was extremely difficult to realize the MIMP SAR observation by a spaceborne SAR [55,56]. However, the concept becomes realistic by a recent advancement of SAR technology, where the ALOS-2, for example, can observe a specific area by the full polarimetric mode in a wider range of incidence angles between 20° and 40° [57].

Nonetheless, collecting MIMP SAR data by only a single satellite is still not very feasible at the present stage because it requires a number of dates in which plant growth potentially affects the data [58,59]. Dominant scattering mechanisms could also be misled by a sparsely sampled incidence angle [60–62]. Multi-incidence angle data can be obtained in another way by assuming uniform vegetation within an entire swath [20,63]. Although it is an efficient way, the assumption could be strict for natural vegetation with widely variable biological parameters. Hence, a direct multi-incidence angle SAR observation by an airborne SAR [32,34,36] was adapted to prevent from all the potential error sources above. Sufficiently small intervals are realized by the repeat path observations so that a time decorrelation can be minimized. The obtained MIMP SAR data are precisely characterized by a theoretical model based on a scattering mechanism. This multiparametric SAR approach improves the polarimetric decompositions to emphasize the sensitivity of backscattering cross section, and optimizes an observation condition for the limited spaceborne SAR monitoring.

A multi-incidence angle observation has been realized by multiple flight paths as proposed by Arii et al. [32,34,36] as shown in Figure 14. The incidence angle is varied to a specific point within the overlapped area by gradually shifting each orbit. For instance, eight observations in every 20 minutes were repeated from noon to 3:00 PM (local time) on August 21, 2014 as described in [32]. Therefore, any external factor such as a meteorological change and vegetation growth could be minimized. The incidence angle at the center of each scene in this study was varied from 24° to 65° by every 6° [27,28,32,34,36].

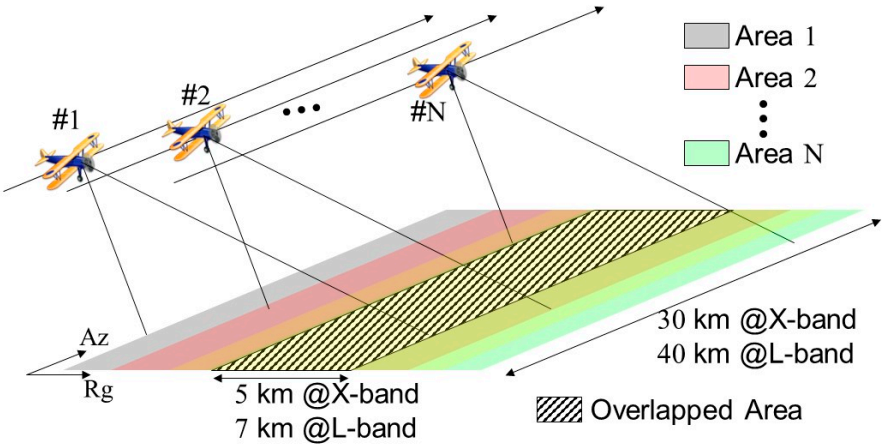

© 2019 IEEE. Reprinted, with permission, from Arii, M.; Yamada, H.; Kojima, S.; Ohki, M. Sensitivity analysis of multifrequency MIMP SAR data from rice paddies. IEEE Trans. Geosci. Remote Sens., 2019, 57, 3543-3551.

Figure 14. Concept of multi-incidence angle observation by an airborne synthetic aperture radar (SAR). Each orbit is gradually varied so that a specific point within the overlapped area has *N* sets of fully polarimetric data in terms of the incidence angle [36].

Currently, a full-polarimetric observation has been common for airborne SAR [64–69] so that the observation can be easily extended to an MIMP SAR observation. In addition, multifrequency MIMP SAR can be realized by simply repeating a set of MIMP SAR flights at a different band. Once multiparametric SAR data are collected, one has to explore simulation parameters as shown in Table 1, which hold for an entire range of observation condition. This concept can be called the comprehensive SAR approach.

Model fitting results are overlapped in Figure 13, and they show excellent agreement so that the selected parameters could be a reliable candidate to describe the backscatter from the paddy fields. This means that the simulated curves of each scattering mechanism shown on the right-hand side of Figure 13 could be also reliable.

As seen above, a history of each scattering mechanism in terms of observation conditions must be essential to quantitative validation of polarimetric decomposition results so that a sensitivity to a particular physical parameter is improved. In addition, a direct inversion from the backscattering cross section could be also feasible [21,24], which could be suitable for spaceborne SAR with a limited chance and observation condition.

4. Conclusions

In this article, the importance of the comprehensive SAR approach and its essential elements was thoroughly reviewed to broaden the use of polarimetric SAR remote sensing.

Popular model-based polarimetric decompositions were first introduced, and their limitations were also discussed with concrete examples, where only qualitative validation has been conducted. A fraction among scattering mechanisms of the backscattering cross section from vegetated surfaces must be essential for quantitative validation. To conquer the problem, a comprehensive SAR approach consisting of two key technologies was thoroughly reviewed.

One element is a forward model. A radiative transfer model and DSM widely used were concisely explained with pros and cons. As an example of the DSM, numerical simulations of backscatter from rice paddies at late vegetative stage were conducted under various observation conditions such as frequency, incidence angle and polarization, and a distinct sensitivity of backscatter to the physical parameters was shown.

The other is the multiparametric SAR observation where a number of SAR observations are conducted by gradually varying observation conditions. A data set of comprehensive SAR observations plays an important role to find reliable DSM parameters holding in a wide range of the observation conditions. Once the model parameters are fixed, a behavior of individual scattering mechanism could be accurately analyzed.

A comprehensive SAR approach consisting of a forward model and multiparametric SAR observation must be essential to move forward a field of polarimetric SAR remote sensing for future operational use.

Author Contributions: Conceptualization, methodology, simulation, M.A.; data analysis, M.A. and H.Y.; validation, H.Y., S.K. and M.O.

Funding: This review paper received no external funding.

Conflicts of Interest: The authors declare no conflict of interest.

References

1. Le Toan, T.; Laur, H.; Mougin, E.; Lopes, A. Multitemporal and dual-polarization observations of agricultural vegetation covers by X-band SAR images. *IEEE Trans. Geosci. Remote Sens.* **1989**, *27*, 709–718. [CrossRef]
2. Zebker, H.A.; van Zyl, J.J.; Durden, S.L.; Norikane, L. Calibrated imaging radar polarimetry: Technique, examples, and applications. *IEEE Trans. Geosci. Remote Sens.* **1991**, *29*, 942–961. [CrossRef]
3. Dubois, P.C.; van Zyl, J.; Engman, T. Measuring Soil Moisture with Imaging Radars. *IEEE Trans. Geosci. Remote Sens.* **1995**, *33*, 916–926. [CrossRef]
4. Dobson, M.C.; Pierce, L.E.; Ulaby, F.T. Knowledge-based land-cover classification using ERS-1/JERS-1 SAR composites. *IEEE Trans. Geosci. Remote Sens.* **1996**, *34*, 83–99. [CrossRef]
5. Le Toan, T.; Ribbes, F.; Wang, L.-F.; Floury, N.; Ding, K.-H.; Kong, J.-A.; Fujita, M.; Kurosu, T. Rice crop mapping and monitoring using ERS-1 data based on experiment and modeling results. *IEEE Trans. Geosci. Remote Sens.* **1997**, *35*, 41–56. [CrossRef]
6. Cloude, S.R.; Pottier, E. An entropy based classification scheme for land applications of polarimetric SAR. *IEEE Trans. Geosci. Remote Sens.* **1997**, *35*, 68–78. [CrossRef]
7. Shi, J.; Wang, J.; Hsu, A.Y.; O'Neil, P.E.; Engman, E.T. Estimation of bare surface soil moisture and surface roughness parameter using L-band SAR image data. *IEEE Trans. Geosci. Remote Sens.* **1997**, *35*, 1254–1266.
8. Pierce, L.E.; Bergen, K.M.; Dobson, M.C.; Ulaby, F.T. Multitemporal land-cover classification using SIR-C/X-SAR imagery. *Remote Sens. Environ.* **1998**, *63*, 24–39. [CrossRef]
9. Hajnsek, I.; Pottier, E.; Cloude, S.R. Inversion of surface parameters from Polarimetric SAR. *IEEE Trans. Geosci. Remote Sens.* **2003**, *41*, 724–744. [CrossRef]
10. Koay, J.-Y.; Tan, C.-P.; Lim, K.-S.; Bakar, S.; Ewe, H.-T.; Chuah, H.-T.; Kong, J.-A. Paddy fields as electrically dense media: Theoretical modeling and measurement comparisons. *IEEE Trans. Geosci. Remote Sens.* **2007**, *45*, 2837–2849. [CrossRef]
11. Lucas, R.; Armston, J.; Fairfax, R.; Fensham, R.; Accad, A.; Carreiras, J.; Bunting, P.; Clewley, D.; Bray, S.; Metcalfe, D.; et al. An evaluation of the ALOS PALSAR L-band backscatter above ground biomass relationship Queensland, Australia: Impacts of surface moisture condition and vegetation structure. *IEEE Trans. Geosci. Remote Sens.* **2010**, *3*, 576–593. [CrossRef]
12. Cloude, S.R. Uniqueness of target decomposition theorems in radar polarimetry. In *Direct and Inverse Methods in Radar Polarimetry*; Part 1, NATO-ARW; Boerner, W.M., Brand, H., Cram, L.A., Holm, W.A., Stein, D.E., Wiesbeck, W., Keydel, W., Giuli, D., Gjessing, D.T., Molinet, F.A., Eds.; Kluwer: Norwell, MA, USA, 1992; pp. 267–296.

13. Van Zyl, J.J. Application of Cloude's target decomposition theorem to Polarimetric imaging radar data. In *Radar Polarimetry*; SPIE-I748; SPIE: Bellingham, WA, USA, 1992; pp. 184–212.
14. Freeman, A.; Durden, S.L. A three-component scattering model for Polarimetric SAR data. *IEEE Trans. Geosci. Remote Sens.* **1998**, *36*, 963–973. [CrossRef]
15. Yamaguchi, Y.; Moriyama, T.; Ishido, M.; Yamada, H. Four-component scattering model for polarimetric SAR image decomposition. *IEEE Trans. Geosci. Remote Sens.* **2005**, *43*, 1699–1706. [CrossRef]
16. Touzi, R. Target scattering decomposition in terms of roll invariant target parameters. *IEEE Trans. Geosci. Remote Sens.* **2007**, *45*, 73–84. [CrossRef]
17. Freeman, A. Fitting a two-component scattering model to polarimetric SAR data from forests. *IEEE Trans. Geosci. Remote Sens.* **2007**, *45*, 2583–2592. [CrossRef]
18. Van Zyl, J.J.; Arii, M.; Kim, Y. Model based decomposition of polarimetric SAR covariance matrices constrained for non-negative eigenvalues. *IEEE Trans. Geosci. Remote Sens.* **2011**, *49*, 3452–3459. [CrossRef]
19. Arii, M.; van Zyl, J.J.; Kim, Y. Adaptive model-based decomposition of polarimetric SAR covariance matrices. *IEEE Trans. Geosci. Remote Sens.* **2011**, *49*, 1104–1113. [CrossRef]
20. Jagdhuber, T.; Hajnsek, I.; Bronstert, A.; Papathanassiou, K.P. Soil moisture estimation under low vegetation cover using a multi-angular polarimetric decomposition. *IEEE Trans. Geosci. Remote Sens.* **2013**, *51*, 2201–2215. [CrossRef]
21. Arii, M. Soil Moisture Retrieval under Vegetation Using Polarimetric Radar. Ph.D. Thesis, California Institute of Technology, Pasadena, CA, USA, 2009.
22. Ishimaru, A. *Wave Propagation and Scattering in Random Media*; IEEE Press: New York, NY, USA, 1978.
23. Bohren, C.F.; Huffman, D.R. *Absorption and Scattering of Light by Small Particles*; John Wiley & Sons: New York, NY, USA, 1983.
24. Van Zyl, J.J.; Kim, Y. *Synthetic Aperture Radar Polarimetry*; Wiley: Hoboken, NJ, USA, 2011.
25. Durden, S.L.; van Zyl, J.J.; Zebker, H.A. Modeling and observations of the radar polarization signatures of forested areas. *IEEE Trans. Geosci. Remote Sens.* **1989**, *27*, 290–301. [CrossRef]
26. Durden, S.L.; Klein, J.D.; Zebker, H.A. Polarimetric radar measurements of a forested area near Mt. Shasta. *IEEE Trans. Geosci. Remote Sens.* **1991**, *29*, 444–450. [CrossRef]
27. Arii, M.; Kitta, H.; Watanabe, T.; Yamada, H. Theoretical study of backscatter from rice paddy using discrete scatterer model. In Proceedings of the Asia-Pacific Conference on Synthetic Aperture Radar (APSAR), Tsukuba, Japan, 23–27 September 2013; pp. 27–30.
28. Arii, M.; Komatsu, T.; Nishimura, T.; Watanabe, T.; Yamada, H.; Kobayashi, T. Theoretical characterization of X-band full polarimetric SAR data from rice paddies in terms of incidence angles. In Proceedings of the IEICE Technical Report, Niigata, Japan, 29 August 2014; Volume 114, pp. 67–72.
29. Arii, M.; Watanabe, T.; Yamada, H. Sensitivity study of radar backscatter from boreal forest using discrete scatter model. In Proceedings of the IEEE International Geoscience and Remote Sensing Symposium, Munich, Germany, 22–27 July 2012; pp. 1425–1428.
30. Watanabe, T.; Yamada, H.; Arii, M.; Park, S.-E.; Yamaguchi, Y. Model experiment of permittivity retrieval method for forested area by using Brewster's angle. In Proceedings of the IEEE International Geoscience and Remote Sensing Symposium, Munich, Germany, 22–27 July 2012; pp. 1477–1480.
31. Watanabe, T.; Yamada, H.; Arii, M.; Sato, R.; Park, S.-E.; Yamaguchi, Y. Study on moisture effects on polarimetric radar backscatter from forested terrain. *IEICE Trans. Commun.* **2014**, *97*, 2074–2082. [CrossRef]
32. Arii, M.; Yamada, H.; Kobayashi, T.; Kojima, S.; Umehara, T.; Komatsu, T.; Nishimura, T. Theoretical characterization of X-band multi-incidence angle and multi-polarimetric SAR data from rice paddies at late vegetative stage. *IEEE Trans. Geosci. Remote Sens.* **2017**, *55*, 2706–2715. [CrossRef]
33. Arii, M.; Yamada, H. Rice paddy monitoring by L-band MIMP SAR Approach. In Proceedings of the IEEE International Geoscience and Remote Sensing Symposium (IGARSS), Fort Worth, TX, USA, 23–28 July 2017; pp. 2442–2445.
34. Arii, M.; Yamada, H.; Ohki, M. Characterization of L-band MIMP SAR data from rice paddies at late vegetative stage. *IEEE Trans. Geosci. Remote Sens.* **2018**, *56*, 3852–3860. [CrossRef]
35. Kim, S.; Arii, M.; Jackson, T. Modeling L-band synthetic aperture radar data through dielectric changes in soil moisture and vegetation over shrublands. *IEEE J. Sel. Top. Appl. Earth Observ. Remote Sens.* **2017**, *10*, 4753–4762. [CrossRef]

36. Arii, M.; Yamada, H.; Kojima, S.; Ohki, M. Sensitivity analysis of multifrequency MIMP SAR data from rice paddies. *IEEE Trans. Geosci. Remote Sens.* **2019**, *57*, 3543–3551. [CrossRef]
37. Arii, M.; van Zyl, J.J.; Kim, Y. A general characterization for polarimetric scattering from vegetation canopies. *IEEE Trans. Geosci. Remote Sens.* **2010**, *48*, 3349–3357. [CrossRef]
38. Borgeaud, M.; Shin, R.T.; Kong, J.A. Theoretical models for polarimetric radar clutter. *J. EM Waves Appl.* **1987**, *1*, 73–91. [CrossRef]
39. Chandrasekhar, S. *Radiative Transfer*; Dover: Mineola, NY, USA, 1960.
40. Ulaby, F.T.; Sarabandi, K.; Mcdonald, K.C.; Whitt, N.W.; Dobson, M.C. *Michigan Microwave Canopy Scattering Model (MIMICS)*; Rep. 022486-T-1; Radiation Laboratory, University of Michigan: Ann Arbor, MI, USA, 1988.
41. Ulaby, F.; Sarabandi, K.; McDonald, K.; Whitt, M.; Dobson, C. Michigan microwave canopy scattering model. *Int. J. Remote Sens.* **1990**, *11*, 1223–1253. [CrossRef]
42. MacDonald, K.C.; Dobson, M.C.; Ulaby, F.T. Using MIMICS to model multiangle and multitemporal backscatter from a walnut orchard. *IEEE Trans. Geosci. Remote Sens.* **1990**, *28*, 477–491. [CrossRef]
43. Dobson, M.C.; Ulaby, F.T. Active microwave soil moisture research. *IEEE Trans. Geosci. Remote Sens.* **1986**, *GE-24*, 23–36. [CrossRef]
44. Tsang, L.; Kong, J.A.; Shin, R. *Theory of Microwave Remote Sensing*; Wiley: New York, NY, USA, 1985.
45. Tsang, L.; Kong, J.A.; Ding, K.H. *Scattering of Electromagnetic Waves*; Vol. 1: Theory and Applications; Wiley: Hoboken, NJ, USA, 2000.
46. Rice, S.O. Reflection of electromagnetic waves from slightly rough surfaces. *Commun. Pure Appl. Math.* **1951**, *4*, 351–378. [CrossRef]
47. Van de Hulst, H.C. *Light Scattering by Small Particles*; Dover: Mineola, NY, USA, 1957.
48. Ruck, G.T.; Barrick, D.E.; Stuart, W.D.; Krichbaum, C.K. *Radar Cross Section Handbook*; Plenum Press: New York, NY, USA, 1970.
49. Ulaby, F.T.; Elachi, C. *Radar Polarimetry for Geoscience Applications*; Artech House: Norwood, MA, USA, 1990; pp. 92–101.
50. Ulaby, F.T.; El-Rayes, M.A. Microwave dielectric spectrum of vegetation-Part II: Dual-dispersion model. *IEEE Trans. Geosci. Remote Sens.* **1987**, *GE-25*, 550–557. [CrossRef]
51. Ribbes, F.; Le Toan, F. Rice field mapping and monitoring with RADARSAT data. *Int. J. Remote Sens.* **1999**, *20*, 745–765. [CrossRef]
52. Oh, Y.; Hong, S.; Kim, Y.; Hong, J.; Kim, Y. Polarimetric backscattering coefficients of flooded rice fields at L- and C-bands: Measurements, modeling, and data analysis. *IEEE Trans. Geosci. Remote Sens.* **2009**, *47*, 2714–2721.
53. Jia, M.; Tong, L.; Chen, Y. Multifrequency and multitemporal ground-based scatterometers measurements on rice fields. In Proceedings of the IEEE International Geoscience and Remote Sensing Symposium, Munich, Germany, 22–27 July 2012; pp. 642–645.
54. El-Rayes, M.A.; Ulaby, F.T. Microwave dielectric spectrum of vegetation-part I: Experimental observations. *IEEE TGRS* **1987**, *GE-25*, 541–549. [CrossRef]
55. Cimino, J.; Casey, A.D.; Rabassa, J.; Wall, S.D. Multiple incidence angle SIR-B experiment over Argentina: Mapping of forest units. *IEEE Trans. Geosci. Remote Sens.* **1986**, *24*, 498–509. [CrossRef]
56. Ahmed, A.; Richards, J.A. Multiple incidence angle SIR-B forest observations. *IEEE Trans. Geosci. Remote Sens.* **1989**, *27*, 586–591. [CrossRef]
57. Arii, M.; Nishimura, T. Landslide monitoring using ALOS-1 and 2 data. In Proceedings of the IEEE International Geoscience and Remote Sensing Symposium (IGARSS), Milan, Italy, 26–31 July 2015; pp. 4129–4132.
58. Shao, Y.; Fan, X.; Liu, H.; Xiao, J.; Ross, S.; Brisco, B.; Brown, R.; Staples, G. Rice monitoring and production estimation using multitemporal RADARSAT. *Remote Sens. Environ.* **2001**, *76*, 310–325. [CrossRef]
59. Lopez-Sanchez, J.M.; Vicente-Guijalba, F.; Ballester-Berman, J.D.; Cloude, S.R. Influence of incidence angle on the coherent copolar polarimetric response of rice at X-band. *IEEE Geosci. Remote Sens. Lett.* **2014**, *12*, 249–253. [CrossRef]
60. Inoue, Y.; Kurosu, T.; Maeno, H.; Uratsuka, S.; Kozu, T.; Dabrowska-Zielinska, K.; Qi, J. Season-long daily measurements of multifrequency (Ka, Ku, X, C, L) and full-polarization backscatter signatures over paddy rice field and their relationship with biological variables. *Remote Sens. Environ.* **2002**, *81*, 194–204. [CrossRef]

61. Lopez-Sanchez, J.M.; Vicente-Guijalba, F.; Ballester-Berman, J.D.; Cloude, S.R. Retrieving rice phenology with X-band co-polar data: A multi-incidence multi-year experiment. In Proceedings of the IEEE International Geoscience and Remote Sensing Symposium (IGARSS), Milan, Italy, 26–31 July 2015; pp. 3977–3980.
62. Cable, J.W.; Kovacs, J.M.; Jiao, X.; Shang, J. Agricultural monitoring in northeastern Ontario, Canada, using multi-temporal polarimetric RADARSAT-2 data. *Remote Sens.* **2014**, *6*, 2343–2371. [CrossRef]
63. Wang, H.; Ouchi, K. Accuracy of the K-distribution regression model for forest biomass estimation by high-resolution polarimetric SAR: Comparison of model estimation and field data. *IEEE Trans. Geosci. Remote Sens.* **2008**, *46*, 1058–1064. [CrossRef]
64. Van Zyl, J.J.; Carande, R.; Lou, Y.; Miller, T.; Wheeler, K. The NASA/JPL three-frequency polarimetric airsar system. In Proceedings of the IEEE International Geoscience and Remote Sensing Symposium, Houston, TX, USA, 26–29 May 1992; Volume I, pp. 649–651.
65. Nadai, A.; Uratsuka, S.; Umehara, T.; Matsuoka, T.; Kobayashi, T.; Satake, M. Development of X-band airborne polarimetric and interferometric SAR with sub-meter spatial resolution. In Proceedings of the IEEE International Geoscience and Remote Sensing Symposium, Cape Town, South Africa, 12–17 July 2009; pp. 913–916.
66. Shimada, M.; Kawano, N.; Watanabe, M.; Motooka, T.; Ohki, M. Calibration and validation of the Pi-SAR-L2. In Proceedings of the Asia-Pacific Conference on Synthetic Aperture Radar (APSAR), Tsukuba, Japan, 23–27 September 2013; pp. 194–197.
67. Shimada, M.; Watanabe, M.; Motooka, T.; Kankaku, Y. PALSAR-2 polarimetric performance and the simulation study using the PI-SAR-L2. In Proceedings of the IEEE International Geoscience and Remote Sensing Symposium, Melbourne, Australia, 21–26 July 2013; pp. 2309–2312.
68. Gebert, N.; Almeida, F.Q.; Krieger, G. Airborne demonstration of multichannel SAR imaging. *IEEE Geosci. Remote Sens. Lett.* **2011**, *8*, 963–967. [CrossRef]
69. Alexander, G.F.; Chapman, B.D.; Hawkins, P.; Hensley, S.; Jones, C.E.; Michel, T.R.; Muellerschoen, R.J. UAVSAR polarimetric calibration. *IEEE Trans. Geosci. Remote Sens.* **2015**, *53*, 3481–3491.

© 2019 by the authors. Licensee MDPI, Basel, Switzerland. This article is an open access article distributed under the terms and conditions of the Creative Commons Attribution (CC BY) license (http://creativecommons.org/licenses/by/4.0/).